Jpn. J. Appl. Phys. Vol. 35 (1996) pp. 2012–2019
Part 1, No. 4A, April 1996

Numerical Study of Single-Electron Resonant Tunnelling via a Few Ionised Donors in Laterally Confined Resonant Tunnelling Diodes

Hiroshi MIZUTA
Central Research Laboratory, Hitachi, Ltd., Kokubunji, Tokyo 185, Japan

(Received December 18, 1995; accepted for publication January 26, 1996)

Single-electron resonant tunnelling (RT) assisted by a few ionised donors is studied for a laterally confined resonant tunnelling diode. The 3D multimode scattering matrix (S-matrix) theory is adopted, introducing the discrete scattering potential of background donors in the active device region. With a few ionised donors placed in the device region, the calculated transmission rate clearly shows new resonances which are dependent on the donor configuration. Visualisation of the electron probability density reveals that these resonances originate in RT via single-donor-induced localised states. This new type of RT leads to *I-V* characteristics with current steps of the order of 0.1 nA per donor before the main current peak, which are in good agreement with experimental results. In addition, the donor-position dependence of the current plateaux and the donor-induced asymmetry of the fine structures are demonstrated.

KEYWORDS: resonant tunnelling, lateral confinement, ionised donor, Schrödinger equation, S-matrix, fine structure

1. Introduction

Laterally confined resonant tunnelling diodes (RTDs) exhibit an interesting interplay between lateral quantisation and Coulomb blockade.[1–4] Recently new in-plane gated AlAs/GaAs/AlAs variable-area resonant tunnelling diodes (VARTDs)[5–7] (see Fig. 1) have been proposed to study the lateral confinement effects on RT. In the VARTDs a graded doping profile in the emitter and collector contact layers and p-type Be^+ ion-implanted gate regions are employed, and so the size of the lateral confinement area can be controlled by applying a negative gate bias to the lateral PN junction. It has been shown that a virtually flat lateral confinement potential is achieved around the double-barrier structure[7] which can prevent complex lateral-mode mixing in the quantum dot.[8] Thus the VARTDs are suitable for investigating the lateral confinement effects on RT systematically. The current-voltage (*I-V*) characteristics have been investigated for the VARTDs with various sizes of emitter pads. A complex fine structure has been observed in the current pinch-off regime of small-area VARTDs with the emitter pad radius of typically 0.7 μm.[6,7] With increasing negative gate bias, i.e. decreasing quantum dot radius, the splitting of the multiple current peaks has been found first to increase for small negative gate voltages and then to remain almost constant for large gate voltages. These characteristic behaviours have been shown to be consistent with the effects of lateral confinement.[6,7]

An additional fine structure has been observed close to the current threshold of relatively large-area VARTDs.[6,7] The *I-V* characteristics for VARTDs with emitter pad radii ranging from 1.0 μm to 2.5 μm show a series of plateau-like structures before a main current peak. The fine structures have been found to be basically independent of the gate bias, i.e. the lateral confinement size, unlike those resulting from the lateral confinement or Coulomb blockade. A possibility of RT through donor states has been pointed out by Dellow *et al.*:[9] an ionised donor in the quantum well will result in a localised potential well and associated bound states which give rise to RT at lower bias voltages than the threshold voltage. Based on this scenario some related quantities are summarised in Table I: the active device area, the active device volume (both estimated for zero gate bias) and the number of donors expected for various sizes of VARTDs under consideration. The total number of donor sites in the GaAs active device region has been estimated from the typical background doping concentration of 10^{14} cm^{-3}. This results in an estimate of from 1 to 5 donor sites, which appears consistent with the proposed scenario. The purpose of this work is to perform a detailed numerical analysis of this phenomenon and to investigate the donor configuration dependence of the *I-V* characteristics.

Table I. Dimensions of the active device regions of the VARTDs and the expected total numbers of ionised donor sites which are estimated from the background donor concentration of 10^{14} cm^{-3} and the active device volumes.

Emitter pad radius (μm)	Active device area (m^2)	Active device volume (m^3)	Estimated number of donors[a)]
1.0	1.0×10^{-12}	0.6×10^{-20}	~ 1
1.5	3.6×10^{-12}	2.1×10^{-20}	~ 2
2.0	7.8×10^{-12}	4.6×10^{-20}	~ 5

a) Assuming background donor concentration of 1×10^{14} cm^{-3}.

2. Three-Dimensional S-Matrix Simulation

This section describes the 3D S-matrix simulation of multimode resonant tunnelling mediated by a few ionised impurities. This simulation method is suitable for investigating the details of the complex tunnelling processes induced by various scattering events and has been applied for two-terminal pillar-type zero-dimensional (0D) RTDs to study the effects of the nonuniform lateral confinement potential.[8] In the present work the theory is extended by introducing the scattering potentials of the random discrete impurities. The formulation is a natural extension of the 1D global coherent tunnelling model[7]

to 3D systems and we start from the 3D time-independent Schrödinger equation:

$$-\frac{\hbar^2}{2m^*}\left(\frac{\partial^2}{\partial x^2}+\frac{\partial^2}{\partial y^2}+\frac{\partial^2}{\partial z^2}\right)\Psi(x, y, z)+V(x, y, z)\Psi(x, y, z)=E\Psi(x, y, z), \tag{1}$$

where $V(x, y, z)$ is the 3D potential distribution which in general consists of the lateral confinement potential, $V_{\mathrm{LC}}(x, y, z)$, the electron affinity, $V_0(z)$, the potential along the channel due to an external bias, $V_{\mathrm{EX}}(z)$, (both assumed to be dependent only on the z-coordinate), and the scattering potentials due to a few ionised impurities, $V_{\mathrm{IM}}(x, y, z)$;

$$V(x, y, z)=V_{\mathrm{LC}}(x, y, z)+V_0(z)+V_{\mathrm{EX}}(z)+V_{\mathrm{IM}}(x, y, z). \tag{2}$$

For simplicity, the Hartree self-consistent potential, $V_{\mathrm{SC}}(x, y, z)$, which will be crucial for discussing the Coulomb blockade effects is neglected in the present work, and $V_{\mathrm{IM}}(x, y, z)$ is modelled by the superposition of the delta functional potential due to the discrete ionised donors:

$$V_{\mathrm{IM}}(\boldsymbol{r})=-V_0\sum_{\{\boldsymbol{r}_{\mathrm{i}}\}}\delta(\boldsymbol{r}-\boldsymbol{r}_{\mathrm{i}}) \tag{3}$$

where $\{\boldsymbol{r}_{\mathrm{i}}\}$ denotes the configuration of the ionised donors. In the following the spatial coordinates of each ionised donor are expressed using lateral and vertical displacements from the centre of the active device region, $(\delta x, \delta y, \delta z)$ (see Fig. 2).

The 3D wavefunction, $\Psi(x, y, z)$, is decomposed using a complete set of 2D lateral eigenstates at each z point, $\varphi_\gamma(x, y|z)$, as follows:

$$\Psi(x, y, z)=\sum_\gamma\varphi_\gamma(x, y|z)\chi_\gamma(z). \tag{4}$$

The z-dependent 2D lateral eigenstates, $\varphi_\gamma(x, y|z)$, are obtained by solving the following 2D Schrödinger equation:

$$-\frac{\hbar^2}{2m^*}\left(\frac{\partial^2}{\partial x^2}+\frac{\partial^2}{\partial y^2}\right)\varphi_\gamma(x, y|z)+V_{\mathrm{LC}}(x, y, z)\varphi_\gamma(x, y|z)=\varepsilon_\gamma(z)\varphi_\gamma(x, y|z) \tag{5}$$

with the Dirichlet boundary conditions on the lateral surface of the device. The index, γ, represents a two-dimensional lateral mode number and $\varepsilon_\gamma(z)$ the corresponding γ-th lateral eigenenergy. For the numerical calculations, the equations are discretised on a 3D finite-difference lattice which has a uniform mesh spacing in the x and y dimensions and a nonuniform spacing in the z dimension.[8] The lateral eigenenergies, $\varepsilon_\gamma(z)$, are obtained from eq. (5) using the bisection method following Householder's tridiagonalisation up to a given energy cut-off: the cut-off energy should be, in general, chosen to be far larger than the Fermi energy in the emitter contact . The corresponding numbers of the eigenstates, $\varphi_\gamma(x, y|z)$, are then calculated by the inverse iteration method. From eqs. (1) and (4), the following 1D scattering equation is derived for $\chi_\gamma(z)$:

$$\frac{\mathrm{d}^2}{\mathrm{d}z_2}\chi_\gamma(z)+k_\gamma^2(z)\chi_\gamma(z)+\sum_{\gamma'}\left(2C_{\gamma,\gamma'}^{(0,1)}(z)\frac{\mathrm{d}}{\mathrm{d}z}\chi_{\gamma'}(z)+C_{\gamma,\gamma'}^{(0,2)}(z)\chi_{\gamma'}(z)-\frac{2m^*}{\hbar^2}V_{\gamma,\gamma'}^{\mathrm{IM}}(z)\chi_{\gamma'}(z)\right)=0 \tag{6}$$

where $k_\gamma(z)$ denotes a complex wave number given by

$$k_\gamma^2(z)=\frac{2m^*}{\hbar^2}(E-\varepsilon_\gamma(z)-V_0(z)-V_{\mathrm{EX}}(z)). \tag{7}$$

Mode mixing coefficients, $C_{\gamma,\gamma'}^{(0,1)}$, $C_{\gamma,\gamma'}^{(0,2)}$, and ionised-donor scattering coefficients, $V_{\gamma\gamma'}^{\mathrm{IM}}(z)$, are written as

$$C_{\gamma,\gamma'}^{(0,1)}(z)=\int\mathrm{d}x\int\mathrm{d}y\varphi_\gamma(x, y|z)\frac{\partial\varphi_{\gamma'}(x, y|z)}{\partial z} \tag{8}$$

$$C_{\gamma,\gamma'}^{(0,2)}(z)=\int\mathrm{d}x\int\mathrm{d}y\varphi_\gamma(x, y|z)\frac{\partial^2\varphi_{\gamma'}(x, y|z)}{\partial z^2} \tag{9}$$

$$V_{\gamma,\gamma'}^{\mathrm{IM}}(z)=\int\mathrm{d}x\int\mathrm{d}y\varphi_\gamma^*(x, y|z)V_{\mathrm{IM}}(x, y, z)\varphi_{\gamma'}(x, y|z) \tag{10}$$

and are evaluated using the obtained set of $\varphi_\gamma(x, y|z)$. The first derivative term of $\chi_\gamma(z)$ in eq. (6) can be eliminated by applying the relevant unitary transformation:

$$\chi_\gamma(z)=\sum_{\gamma'}M_{\gamma,\gamma'}(z)f_{\gamma'}(z) \tag{11}$$

where the unitary matrix, $M_{\gamma\gamma'}(z)$, is defined as follows:

$$M_{\gamma,\gamma'}(z)=\exp\left(-\int^z C_{\gamma,\gamma'}^{(0,1)}(z')\mathrm{d}z'\right). \tag{12}$$

The matrix $M_{\gamma,\gamma'}(z)$ is calculated using a second-order expansion approximation[10] which guarantees the unitarity

of the matrix. Substituting eqs. (11) and (12) into eq. (6), the transformation leads to the following equation:

$$\frac{\mathrm{d}^2}{\mathrm{d}z^2} f_\gamma(z) = -\sum_{\gamma'} \omega_{\gamma,\gamma'}(z) f_{\gamma'}(z) \tag{13}$$

where the matrix, $\omega_{\gamma,\gamma'}(z)$, is written as follows:

$$\omega_{\gamma,\gamma'}(z) = \sum_{\gamma''}\sum_{\gamma'''} (M^{-1})_{\gamma,\gamma''}(z) W_{\gamma'',\gamma'''}(z) M_{\gamma''',\gamma'}(z) \tag{14}$$

$$W_{\gamma,\gamma'}(z) = k_\gamma^2(z)\delta_{\gamma,\gamma'} - \{C^{(0,1)}(z)\}^2_{\gamma,\gamma'} - C^{(1,1)}_{\gamma,\gamma'}(z) - \frac{2m^*}{\hbar^2} V^{\mathrm{IM}}_{\gamma,\gamma'}(z) \tag{15}$$

$$C^{(1,1)}_{\gamma,\gamma'}(z) = \int \mathrm{d}x \int \mathrm{d}y \frac{\partial \varphi_\gamma(x, y|z)}{\partial z} \frac{\partial \varphi_{\gamma'}(x, y|z)}{\partial z}. \tag{16}$$

Renormalised complex wave numbers, $K_\gamma(z)$, which include the lateral mode mixing, are obtained by solving the eigenvalue equation:

$$\sum_{\gamma''} W_{\gamma,\gamma''}(z) V_{\gamma'',\gamma'}(z) = \{K_{\gamma'}(z)\}^2 V_{\gamma,\gamma'}(z) \tag{17}$$

where $V_{\gamma,\gamma'}(z)$ is a unitary matrix which diagonalises the matrix $W_{\gamma,\gamma'}(z)$. The eigenvalue equation (17) is discretised and numerically solved using the QL method. Then the z-component of the wavefunction can be expressed as a superposition of plane waves:

$$\chi_\gamma(z) = \sum_{\gamma'}\sum_{\gamma''} M_{\gamma,\gamma'}(z) V_{\gamma',\gamma''}(z) \{A_{\gamma''}(z)\exp(iK_{\gamma''}(z)z) + B_{\gamma''}(z)\exp(-iK_{\gamma''}(z)z)\} \tag{18}$$

where $A_\gamma(z)$ and $B_\gamma(z)$ are coefficients of forward and backward plane waves in the γ-th lateral mode with the complex wave number, $K_\gamma(z)$. Assuming these coefficients to be constant between two adjacent z-mesh points, the three-dimensional wavefunction, $\Psi(x, y, z)$, can be finally written as

$$\Psi^{(i)}(x, y, z) \cong \sum_{\gamma}\sum_{\gamma'}\sum_{\gamma''} \varphi_\gamma(x, y|z) M^{(i)}_{\gamma,\gamma'} V^{(i)}_{\gamma',\gamma''} \{A^{(i)}_{\gamma''}\exp(iK^{(i)}_{\gamma''}z) + B^{(i)}_{\gamma''}\exp(-iK^{(i)}_{\gamma''}z)\} \tag{19}$$

where the index, (i), denotes the small region between adjacent z-mesh points, z_i and z_{i+1}. The lateral-mode-based transfer matrix and hence the S-matrix are then defined from the continuity of electron probability flux of electrons.[8] The total transmission rate is obtained by summing up all the contributions from the lateral modes and then the tunnelling current is finally calculated assuming global coherent tunnelling.[8]

3. Results and Discussions

The numerical simulation was performed for a relatively large-area VARTD with the active device region composed of a symmetric AlAs(4.2 nm)/GaAs(5.6 nm)/AlAs(4.2 nm) double-barrier structure: the layer thicknesses are the same as those used in the experiments reported in ref. 6. In the previous study of the conventional 0D RTDs[8] the complex lateral confinement potential profiles, $V_{\mathrm{LC}}(x, y, z)$, which are formed by the non-uniform surface depletion along the etched pillar surface were determined using a classical device simulation incorporating Spicer's surface trap model. For the present VARTDs, however, it has been shown that a virtually flat lateral confinement is in fact achieved around the double-barrier structure.[7] Thus, in the present work, only the essential active device region is focused on and lateral confinement is assumed to be completely flat. The confinement profile is simply modelled using a square well 200 nm in diameter in which the intervals of lateral eigenenergies are so small that contributions from differ-

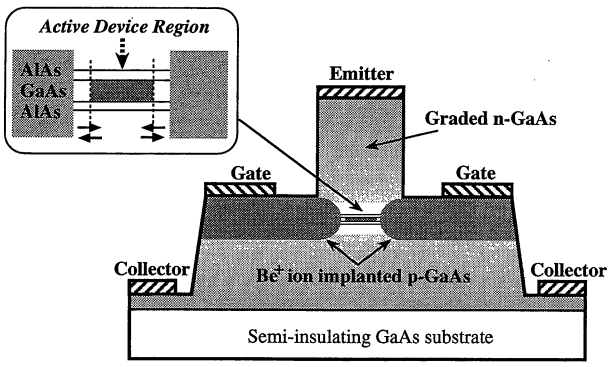

Fig. 1. Schematic cross section of a VARTD and a variable-size active device region formed by a vertical AlAs/GaAs/AlAs double-barrier structure and a lateral PN-junction. Pseudo-uniform lateral confinement potential is controlled by gate electrodes.

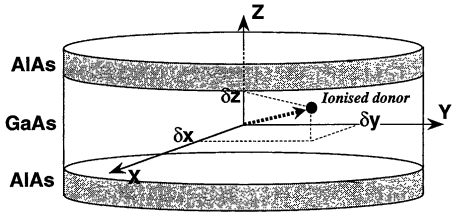

Fig. 2. Three-dimensional spatial coordinates of ionised donors in the active device region. The position of a single ionised donor is described by its displacement, $(\delta x, \delta y, \delta z)$, from the centre of the region.

ent modes are barely separable on the I-V curve. Therefore the present situation allows us to concentrate purely on the effects of the random ionised donors located in the active device region.

We first examine the VARTD in which two ionised donors are placed. Figure 3(a) shows the energy dependence of the total transmission rate, $T(E)$, for an emitter-collector voltage of 175 mV. In this case one donor is at the centre of the active device region, $(\delta x, \delta y, \delta z) = (0, 0, 0)$ and the other at $(\delta x, \delta y, \delta z) = (48\,\text{nm}, 48\,\text{nm}, 1.3\,\text{nm})$. In the high-energy region we see a series of transmission peaks which are very close to each other. These transmission peaks represent RT through the original quantised states whose energy intervals are

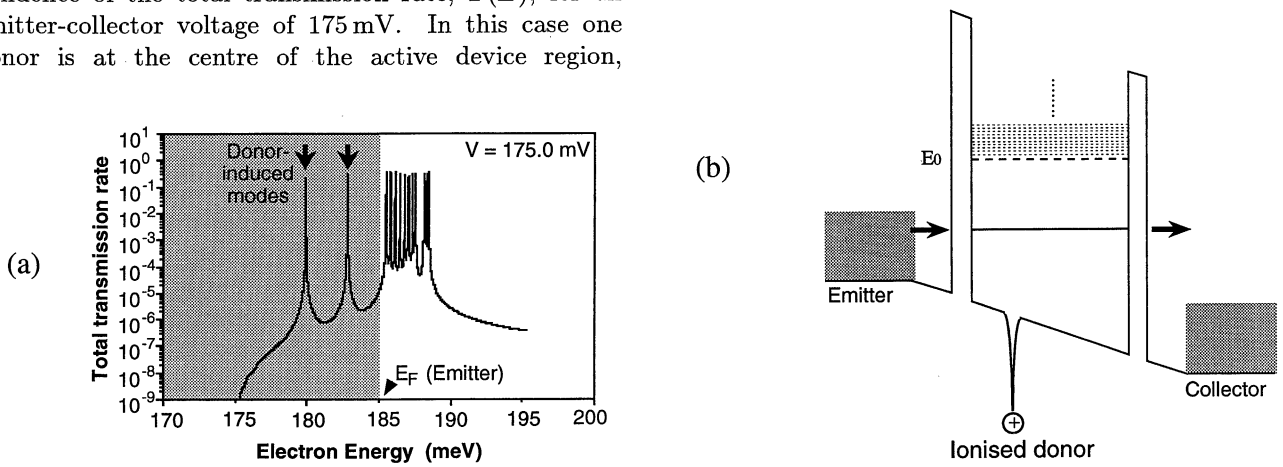

Fig. 3. (a) Electron energy dependence of total transmission rate, $T(E)$, calculated for a VARTD including two ionised donors: one is at $(0, 0, 0)$ and the other at $(48\,\text{nm}, 48\,\text{nm}, 1.3\,\text{nm})$. The gray region represents the Fermi sea in the emitter. The applied emitter-collector voltage is 175.0 mV which corresponds to the main current threshold voltage of the VARTD (see the I-V characteristics in Fig. 5). (b) A schematic energy band diagram for the single-donor-induced RT. The broken line labelled E_0 is the lowest quasi-bound state of the double-barrier structure and the dotted lines are the virtually degenerate 3D quantised states of the active device region. The solid line at a lower energy represents the single-electron RT state induced by an ionised donor.

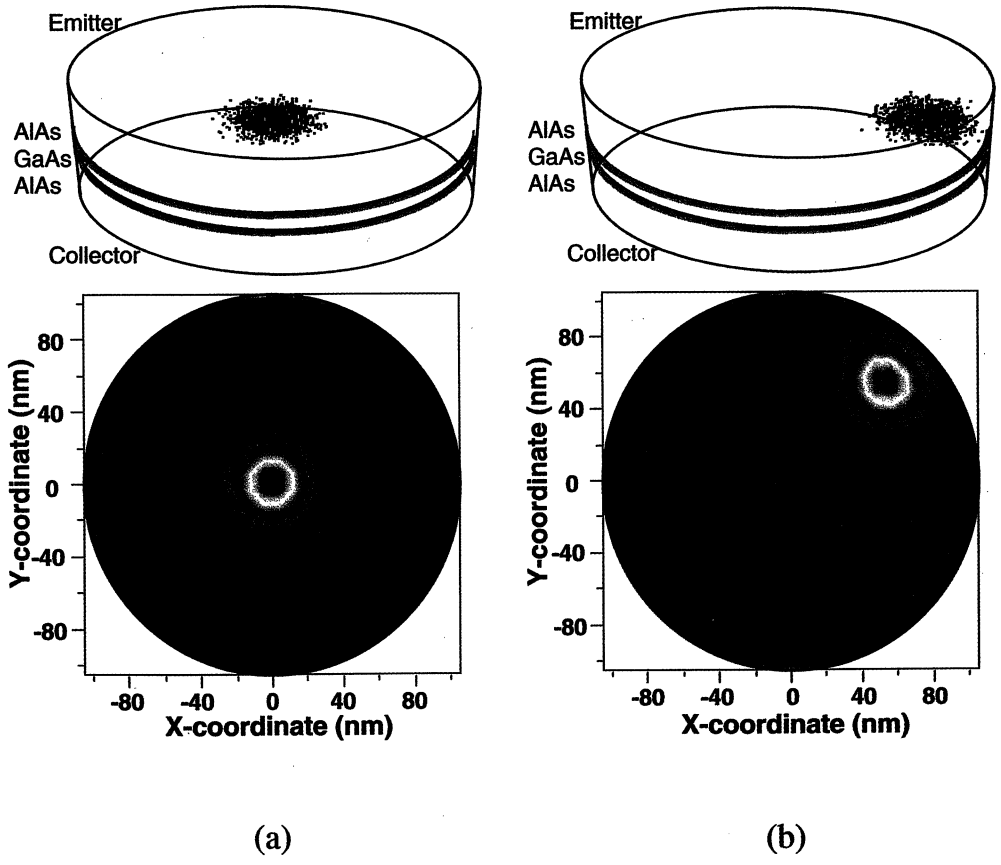

Fig. 4. Visualised 3D and 2D probability densities of electrons, $|\Psi(x, y, z)|^2$, in the VARTD including two ionised donors calculated for the first-mode incident wave from the emitter, at electron energies of (a) 177.9 meV (1st resonance) and (b) 182.8 meV (2nd resonance) corresponding to the first two peaks in Fig. 3(a). The 2D visualisations show the in-plane distribution in the middle of the quantum well, $|\Psi(x, y, 0)|^2$.

determined by the size of the lateral confinement and which are thus nearly degenerate since the confinement size is chosen to be fairly large. These peaks simply give rise to a large single negative differential conductance (NDC) in the *I-V* characteristics (see Main peak in Fig. 5(a)) in the same way as in conventional RTDs. In addition to these peaks, two transmission peaks are seen in Fig. 3(a) at lower energies (indicated with arrows) which are isolated from the peaks at higher energies. These new peaks result from the ionised donors embedded in the active device region: the attractive potential of each ionised donor selectively pulls down one of the degenerate states to lower energy. Figure 3(b) depicts the schematic energy band diagram along a vertical channel when an ionised donor is introduced in the active device region: E_0 denotes the lowest quasi-bound state of the quantum well (a broken line) and the nearly degenerate states are shown by dotted lines above E_0. The lower single solid line represents the single-donor-induced state through which electrons tunnel from the emitter to the collector. Which state is chosen is determined by both the position of the ionised donor and the spatial distribution of the original eigenstate. This may be understood from the probability densities of electrons calculated at these two resonant energies. Figure 4 shows the visualised 3D and 2D probability densities, $|\Psi(x, y, z)|^2$, at (a) 1st and (b) 2nd resonances calculated for the lowest 1st-mode incident waves from the emitter. The 2D pictures show the in-plane amplitude at $z = 0$, $|\Psi(x, y, 0)|^2$. It can be seen that the electron probability densities are strongly localised around the different ionised donor sites although the incident wave spreads laterally over the whole area at the emitter edge.

These transmission characteristics lead to the *I-V* characteristics for the VARTD shown in Fig. 5 calculated at 4.2 K for (a) an extended bias region and (b) around the current threshold. As mentioned earlier the series of transmission peaks at higher energies result in the large NDC around $V = 185$ mV as seen in Fig. 5(a). On the other hand it is found that the ionised-donor-induced transmission peaks seen in Fig. 3(a) lead to two current plateaux with a step of about 0.1 nA before the main NDC. Obviously the details of these current plateaux depend on the donor configuration, and the *I-V* curve shown here is just for one particular configuration. However it should be noted that the simulated current step of 0.1 nA corresponds well to the experimental results.[6,7] This is because the value of the single current step is essentially determined by the width of the corresponding transmission peak, i.e. the dwell time[7] of electrons at the resonant state, which is mainly determined by the layer thicknesses of the AlAs/GaAs/AlAs double-

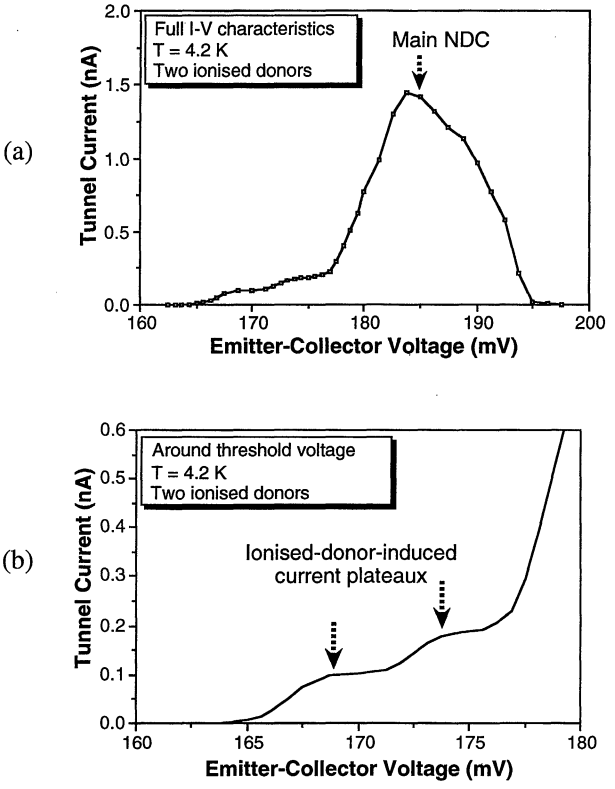

Fig. 5. *I-V* characteristics calculated at 4.2 K for the VARTD including two ionised donors: (a) full characteristics and (b) detail around the threshold voltage.

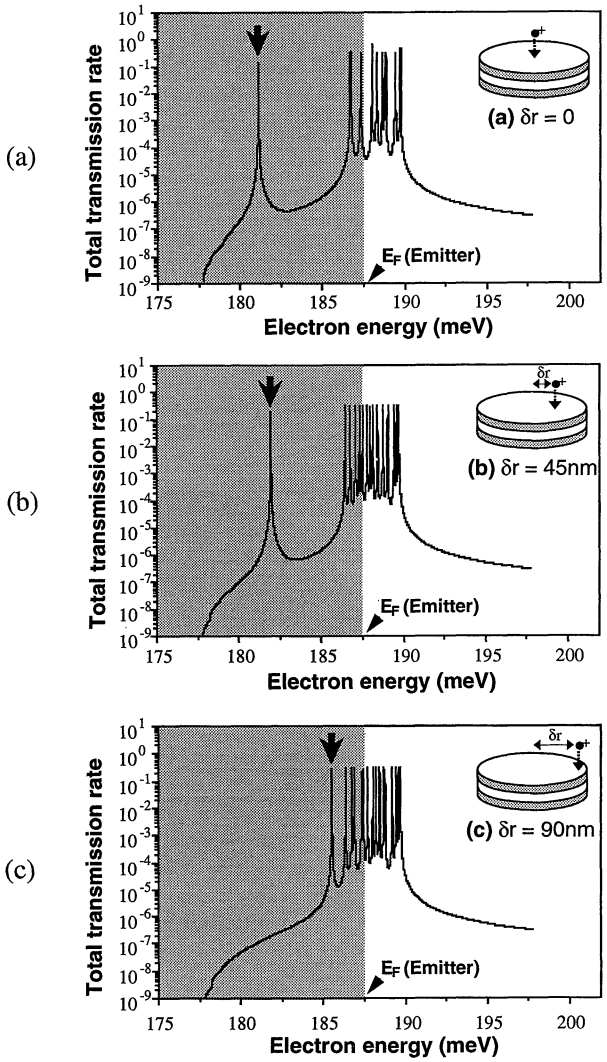

Fig. 6. Transmission rate calculated for VARTDs with a single ionised donor placed at various in-plane positions (see the insets): (a) at the centre, (b) at $\delta r(\equiv \sqrt{\delta x^2 + \delta y^2}) = 45$ nm and (c) at $\delta r = 90$ nm ($\delta z = 0$). The emitter-collector bias is 177.5 mV.

barriers. The step current, I, may be given by the following simple formula for single-electron RT:

$$I = e/\tau_{\mathrm{d}} \tag{20}$$

where τ_{d} is the associated electron dwell time at the resonant energy. Using eq. (20) and the obtained step current of 0.1 nA, τ_{d} is estimated to be about 1500 ps. This is theoretically equivalent to an estimate based on the simulated width of the transmission peak in Fig. 3(a) and the uncertainty principle.[7] The dwell time of this VARTD has also been evaluated for a large-area sample using magnetoconductance measurements.[7,11] The evaluation is based on the following formula for the normal RT current density, J:

$$J = e\sigma_{\mathrm{w}}/\tau_{\mathrm{d}}^{0} \tag{21}$$

where σ_{w} is the sheet concentration of electrons accumulated in the quantum well at resonance. Measurements were conducted to estimate σ_{w} at the main resonance of the RTD, and the value of about $10^{11}\,\mathrm{cm}^{-2}$ was obtained.[7,11] This gives a τ_{d}^{0} value of about 500 ps which is slightly smaller than the τ_{d} obtained above. Strictly speaking, τ_{d} in eq. (20) is not the same as τ_{d}^{0} in eq. (21) since the energies of the relevant resonant states are now

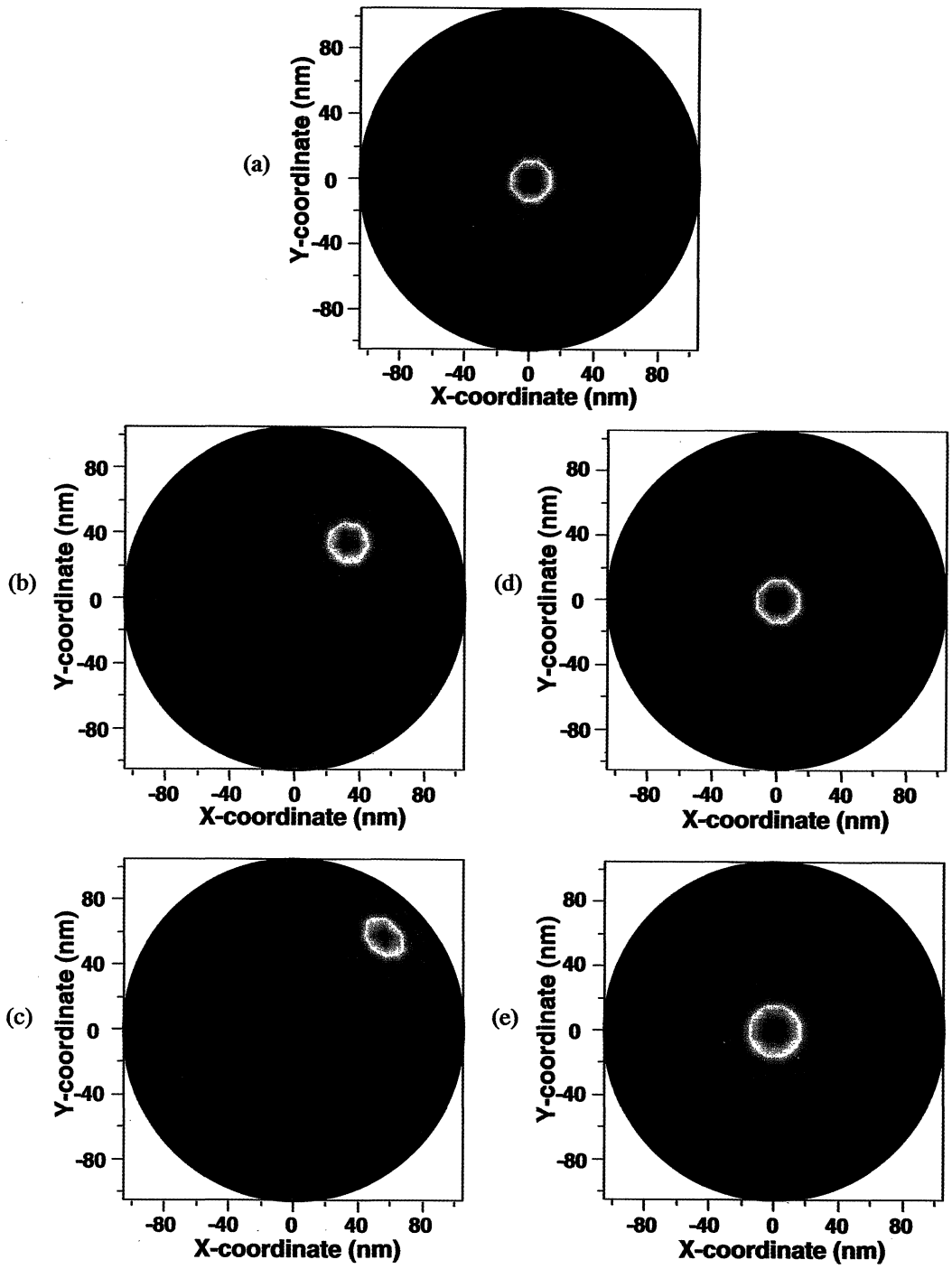

Fig. 7. Two-dimensional probability density of electrons at resonance calculated for VARTDs with a single ionised donor at various locations in the active device regions: (a) at the centre, (b) at $(\delta r, \delta z) = (45\,\mathrm{nm}, 0\,\mathrm{nm})$, (c) at $(\delta r, \delta z) = (90\,\mathrm{nm}, 0\,\mathrm{nm})$, (d) at $(\delta r, \delta z) = (0\,\mathrm{nm}, 1.8\,\mathrm{nm})$ and (e) at $(\delta r, \delta z) = (0\,\mathrm{nm}, 2.75\,\mathrm{nm})$.

slightly shifted to lower energy as we saw in Figs. 3(a) and 3(b). Thus the associated dwell time τ_d is thought to increase slightly, although this change should be quite small since energy shift of the order of 10 meV is much smaller than the original energy depth, 0.956 eV, of the AlAs/GaAs/AlAs quantum well. The τ_d value obtained above seems to be consistent with these considerations, and this also indicates that the observed current step is attributable to the present mechanism.

Next let us investigate how the fine structure of the I-V characteristics depends on the location of the ionised donor in the active device region. To manifest this, VARTDs including only a single ionised donor are also simulated with both vertical and lateral motion of the single donor in the active device region. Figures 6(a)–6(c) show the change in the transmission rate, $T(E)$, when the single ionised donor is moved laterally from the centre to the edge of the region. The vertical coordinate of the donor is kept constant, i.e. $\delta z = 0$. It is found that the single transmission peak induced by the single ionised donor gradually shifts to higher energy and finally merges into the series of peaks. This is because the interactions between the single ionised donor and the tunnelling electrons are essentially determined by the overlap of the original lateral wavefunctions with the local potential profiles. As the single donor moves towards the edge the amplitude of the original lateral wavefunction at the donor site decreases and the attractive potential of the donor has less effect on the electron state. Therefore the energy interval between the single-donor-induced transmission peak and the high-energy peaks is at its maximum when the donor is located at the centre of the device and is gradually reduced as the donor site is displaced from the center. The electron probability density at the resonance varies as shown in Figs. 7(a)–7(c) in the 2D representation. It can be seen that the localised electron probability density also changes its in-plane distribution with the shift of the donor. In the same manner the $T(E)$ curves for vertical shift of the ionised donor are shown in Figs. 8(a)–8(c), and the corresponding in-plane probability densities are depicted in Figs. 7(a), 7(d) and 7(e). This time the donor is moved in the quantum well towards the AlAs barrier on the emitter side while its lateral coordinates are fixed at the centre of the area, $(\delta x, \delta y) = (0, 0)$. The change in $T(E)$ is quite similar to that for the lateral displacement shown in Fig. 6. However, the electron probability density varies in a different manner as seen in Fig. 7. In this case the centre of the probability density is obviously fixed at the centre of the active device area, but the whole distribution gradually spreads out over the area. This means that when the donor is placed closer to the emitter barrier the attractive potential has less influence on the electron state. This is because the overlap of the vertical component of the original wavefunction with the localised donor potential decreases greatly as the donor shifts from the center towards the emitter.

As a result the single current plateau around the threshold voltage changes as shown in Fig. 9 for (a) the lateral displacement of the donor and (b) the vertical displacement. In both cases, as the single donor moves

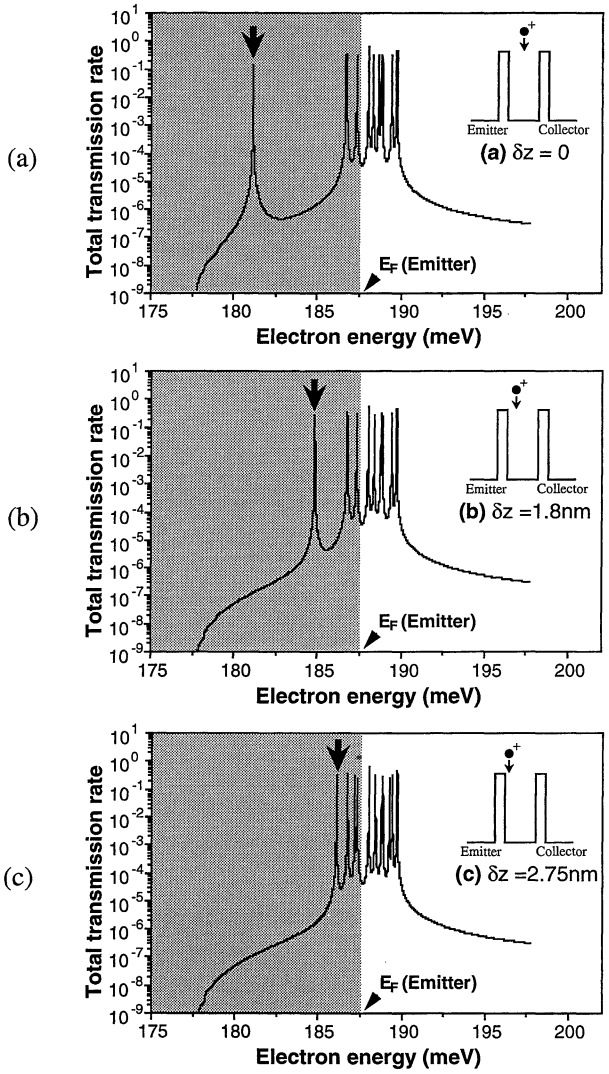

Fig. 8. Total transmission rate calculated for VARTDs with a single ionised donor placed at various vertical positions (see the insets): (a) at the centre, (b) at $\delta z = 1.8$ nm and (c) at $\delta z = 2.75$ nm ($\delta x = \delta y = 0$).

from the centre to the edge of the region either laterally or vertically, the subthreshold voltage of the single current plateau shifts towards the main peak voltage while the current step remains virtually the same. In the case of multiple ionised donors, therefore, the fine structure will be given by a superposition of the current plateaux and so will be donor-configuration-dependent. From these results we expect that the I-V fine structures in general should differ in the forward and reverse emitter-collector bias directions even though the original AlAs/GaAs/AlAs double-barrier is symmetrical. As an example we show in Fig. 10 the I-V curve calculated for the same VARTDs including two ionised donors but for the reverse emitter-collector bias direction: the details of the current plateaux are found to be different from those in Fig. 5(a). This phenomenon is observed in experiments[6,7] and this also supports the validity of the present mechanism.

4. Conclusion

We have presented the theoretical analysis of few-

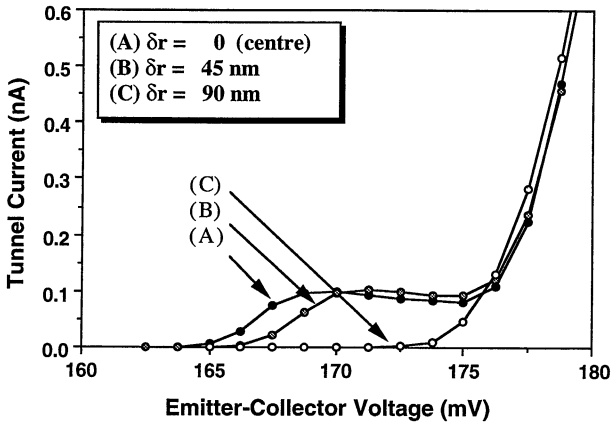

(a)

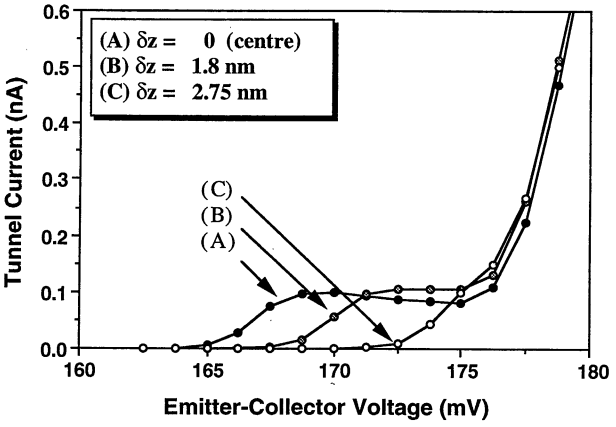

(b)

Fig. 9. Details of *I-V* curves around the threshold voltage calculated for VARTDs with various locations of a single ionised donor: (a) for lateral displacement and (b) for vertical displacement.

ionised-donor-induced RT based on the 3D multimode S-matrix simulation. Introducing the discrete ionised donor scattering potential, numerical simulation has been conducted for large-area VARTDs with various configurations of ionised donors. The calculated energy dependence of the total transmission rate shows new transmission peaks at lower energies than the conventional RT transmission peaks and those resonant energies have been found to be strongly dependent on the configuration of the ionised donors. The simulated current plateaux and associated electron dwell time have been shown to be consistent with experimental results. The donor position dependence of the current fine structure has also been investigated by moving a single ionised donor vertically and horizontally. It has been revealed that the subthreshold voltage of the current plateau is sensitive to the displacement of the donor and so leads to donor-

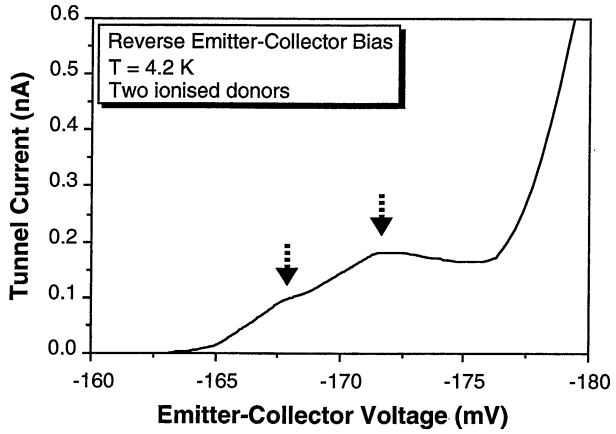

Fig. 10. *I-V* characteristics under reverse emitter-collector bias calculated for the VARTD including two ionised donors in the same configuration as that used for Fig. 5.

configuration-dependent asymmetry in the *I-V* characteristics, which is also consistent with the results of experiments.

Acknowledgements

The author wishes to thank Dr. C. J. Goodings (now at Philips Research Laboratories, Redhill, U.K.), Dr. J. R. A. Cleaver, Professor H. Ahmed of the Microelectronics Research Centre, University of Cambridge, Dr. K. Nakazato of Hitachi Cambridge Laboratory, Hitachi Europe Ltd., and Dr. T. Teshima and Dr. K. Yamaguchi of Central Research Laboratory, Hitachi Ltd., for invaluable discussions.

1) Bo Su, V. J. Goldman and J. E. Cunningham: Phys. Rev. B **46** (1992) 7644.
2) M. Tewordt, L. Martin-Moreno, J. T. Nicholls, M. Pepper, M. J. Kelly, V. J. Law, D. A. Ritchie, J. E. F. Frost and G. A. C. Jones: Phys. Rev. B **45** (1992) 14407.
3) P. Guéret, N. Blanc, R. German and H. Rothuizen: Phys. Rev. Lett. **68** (1992) 1896.
4) S. Tarucha, T. Honda, T. Saku and Y. Tokura: Surf. Sci. **305** (1994) 547.
5) C. J. Goodings, H. Mizuta, J. R. A. Cleaver and H. Ahmed: Surf. Sci. **305** (1994) 353.
6) C. J. Goodings, H. Mizuta, J. R. A. Cleaver and H. Ahmed: J. Appl. Phys. **76** (1994) 1276.
7) H. Mizuta and T. Tomonori: *The Physics and Applications of Resonant Tunnelling Diodes* (Cambridge University Press, Cambridge, 1995), Chaps. 4 and 6.
8) H. Mizuta, C. J. Goodings, M. Wagner and S. Ho: J. Phys.: Condens. Matter **4** (1992) 8783.
9) M. W. Dellow, P. H. Beton, C. J. G. M. Langerak, T. J. Foster, P. C. Main, L. Eaves, M. Henini, S. P. Beaumont and C. D. W. Wilkinson: Phys. Rev. Lett. **68** (1992) 1754.
10) K. Nakazato and R. J. Blaikie: J. Phys.: Condens. Matter **3** (1991) 5729.
11) C. J. Goodings, H. Mizuta and J. R. A. Cleaver: J. Appl. Phys. **75** (1994) 2291.